Cell Reports, Volume *23*

Supplemental Information

Rapid Neuromodulation of Layer 1 Interneurons in Human Neocortex

Rogier B. Poorthuis, Karzan Muhammad, Mantian Wang, Matthijs B. Verhoog, Stephan Junek, Anne Wrana, Huibert D. Mansvelder, and Johannes J. Letzkus

Supplemental Information

Supplemental Figures

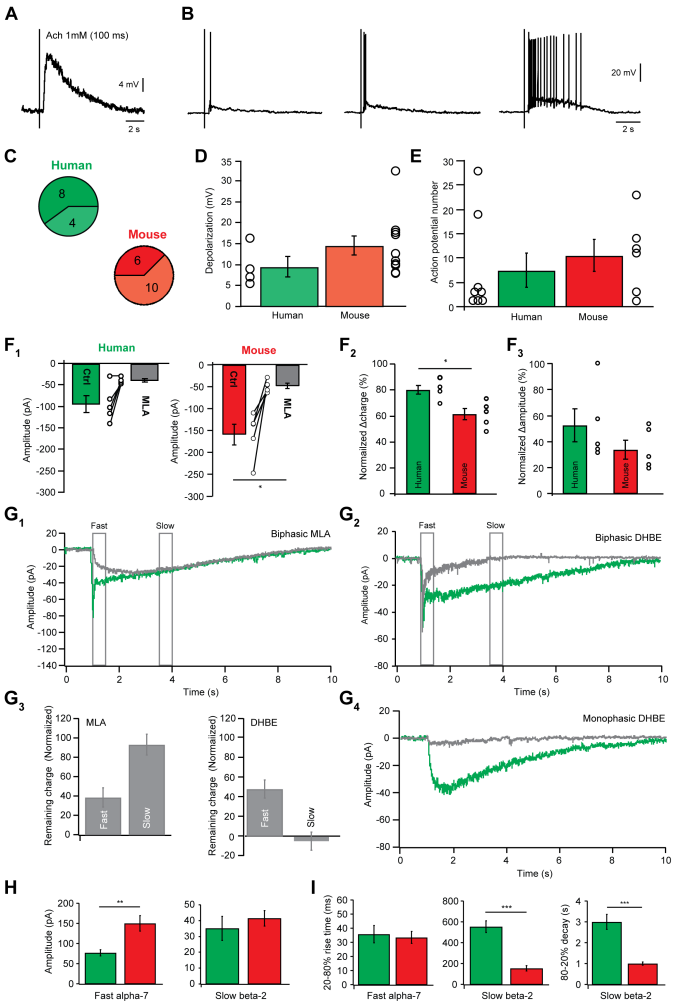

Figure S1: Nicotinic voltage responses and pharmacology of human and mouse layer 1 interneurons. Related to Figure 1.

Example subthreshold (**A**) and suprathreshold voltage responses in human L1-INs (**B**). **C** Proportion of subthreshold (light color) and suprathreshold (dark color) responses in human (green) and mouse L1-INs (red). **D** Average amplitude of subthreshold responses in human (n=4, 9.56±2.4 mV) and mouse L1-INs (n=10, 14.6±2.2 mV, p=0.09, Kruskal-Wallis test). **E** Number of action potentials elicited in human (n=8, 7.5±3.6 APs) and mouse L1-INs (n=6, 10.7±3.3 APs). These data indicate similar recruitment of L1-INs in the two species by acetylcholine. **F_1** The selective α7 receptor antagonist MLA (10 nM) strongly reduced the peak amplitude of biphasic nicotinic currents in human (n=5, p=0.06, Wilcoxon signed rank test, 94.1±8.8 versus 40.0±3.2 pA) and mouse L1-INs (n=5, p=0.01, Wilcoxon signed rank test, 159.1±24.1 versus 48.0±6.2 pA). **F_2** The MLA-sensitive α7 receptor response contributed relatively less charge to biphasic currents in human compared to mouse (p=0.01, Kruskal-Wallis test, n=5 each, 79.9±3.2 versus 61.8±4.5%). **F_3** In contrast, the relative amplitude was affected similarly in the two species (p=0.17, Kruskal-Wallis test, n=5 each, 52.6±12.9 versus 33.2±7.0%). **G_1** Average trace (n=5 neurons) displaying the effect of MLA on biphasic

currents in human cells. MLA strongly reduces the charge in the early phase of the nicotinic current but not in the late phase, consistent with the kinetics of α7 nicotinic receptors that are characterized by a fast activation onset and rapid desensitization. **G_2** Average trace (n=3) displaying the effect of DHBE on biphasic currents. DHBE strongly reduces the late component of human nicotinic currents while leaving the rapid component intact, indicating that the late component is mediated by β2-containing nicotinic receptors that are characterized by slow kinetics. **G_3** Quantification of the effect of MLA and DHBE on the early and late component of nicotinic currents indicated in **G_1** and **G_2**. MLA greatly reduced the charge in the early phase (38.4±9.9 % remaining charge) but did not affect the late phase of the current (93.5±10.6 % remaining charge). DHBE also effected the early phase of the nicotinic current (47.7±9.6% remaining charge), indicating that consistent with the trace in **G_1**, at this time point the response is mediated by both receptor types. In contrast to MLA, however, DHBE completely abolished the late component (-5.41±9.1% remaining charge). These data indicate that a subset of human layer 1 neurons expresses two different types of nicotinic receptors. **G_4** Complete block of slow monophasic responses in human cells (n=4) by DHBE. **H** The amplitude of α7 currents was larger in mouse compared to human L1-INs (left, p<0.01, Kruskal-Wallis test, human n=13, mouse n=28, 77.0±7.2 versus 150.5±19.5 pA). In contrast, β2-containing receptor currents displayed similar amplitudes in both species (right, p=0.70, Kruskal-Wallis test, human n=8, mouse n=18, 35.2±7.4 versus 41.4±4.9 pA). **I** The rise time of α7 currents did not differ between human and mouse L1-INs (left, p=0.99, Kruskal-Wallis test, human n=13, mouse n=28, 35.8±6.3 versus 33.6±4.3 ms). In contrast, β2-containing receptor currents displayed both slower rise (center, p<0.001, Kruskal-Wallis test, human n=8, mouse n=18, 554.5±75.4 versus 165.3±25.4 ms) and decay times in human recordings (right, p<0.001, Kruskal-Wallis test, human n=18, mouse n=43, 2.88±0.33 versus 1.01±0.08 s). This difference may be due to differential modulation of receptor kinetics, differential sub-cellular localization of the receptors or differences in L1-IN morphologies between the species. Error bars indicate s.e.m.

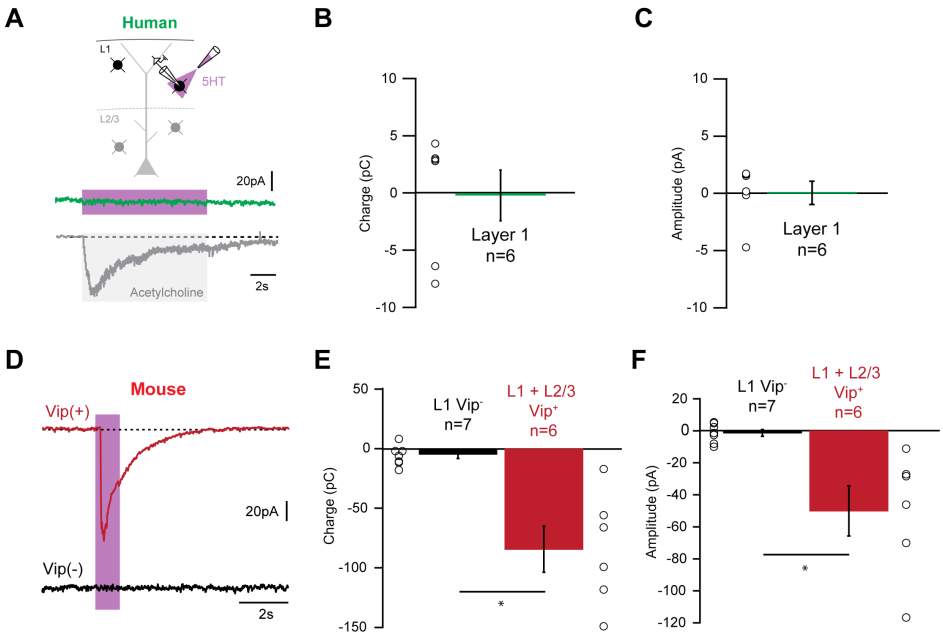

Figure S2: Serotonin responses in human and mouse layer 1 interneurons. Related to Figure 2.

A Experimental setup for pressure application of 5-HT (100 µM) for 10s. 5-HT elicited no detectable response in human L1-INs (**B**, **C**, n=6), in contrast to robust responses when acetylcholine was applied to the same cells (inset in **A**, 10s application). **D** Example responses of a Vip positive and a Vip negative L1-IN to 5-HT (1s, 100 µM). While Vip negative L1-INs showed no response, Vip positive interneurons in layer 1 and layer 2/3 displayed large inward currents. **E** The average charge of 5-HT responses in Vip negative L1-INs was -4.69±3.63 pC (n=7), whereas Vip positive interneurons in layer 1 and layer 2/3 displayed responses of -84.35±19.43 pC (n=6, $p<0.01$, Kruskal-Wallis test). **F** The average amplitude of 5-HT responses in Vip negative L1-INs was -1.32±2.14 pA (n=7), whereas Vip positive interneurons in layer 1 and layer 2/3 displayed responses of -50.08±15.68 pA (n=6, $p<0.01$, Kruskal-Wallis test). Together with data in **Figure 2**, this indicates that within layer 1, 5-HT controls exclusively the small population of interneurons that expresses Vip. Error bars indicate s.e.m.

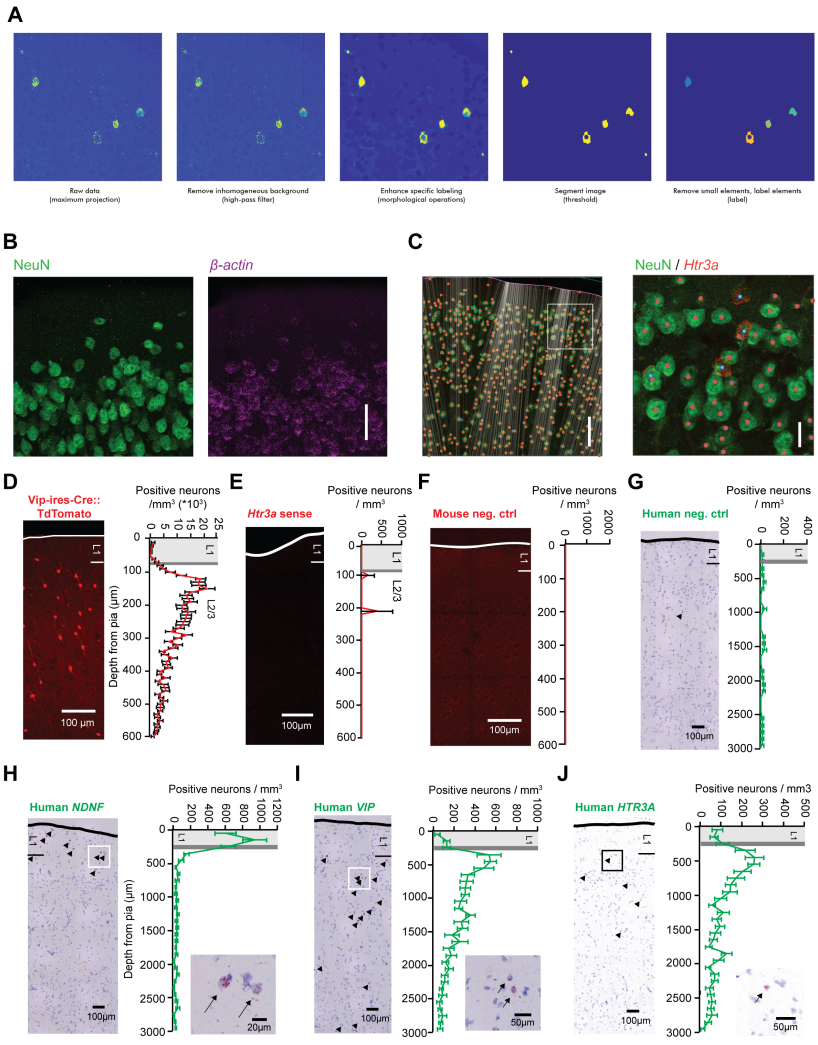

Figure S3: In situ hybridization for HTR3A receptors, VIP and NDNF in human and mouse temporal cortex. Related to Figure 2 and 4.

A Operations performed on fluorescent *in situ* images to convert the punctate staining to identification of positive neurons (see Methods for details). **B** Slice of mouse temporal cortex showing layer 1 and layer 2/3 neurons stained for the neuronal marker NeuN (**left**) and β-actin mRNA (**right**). Note detection of mRNA in layer 1 neurons (scale bar 50 µm). **C left** Neurons were automatically detected in the NeuN channel, and their distance to the pia was determined by drawing a line to the closet point on the pia (scale bar 100 µm). **C right** Automatically detected neurons in the NeuN channel are depicted as red dots. *Htr3a* mRNA positive cells detected by the analysis algorithm are labeled with a blue dot. The punctate mRNA staining was fused by the operation shown in **A** to identify positive neurons in an unbiased fashion (scale bar 20 µm). **D right** Vip interneurons were visualized using Vip-ires-cre mice (Taniguchi et al., 2011) crossed with a tdTomato reporter line (Ai9, Madisen et al., 2010). **Left** Density of Vip interneurons as a function of distance from the pia (n=3 mice, 29 slices). **E** Control experiment with a sense probe for *Htr3a* receptor mRNA showed virtually no false positive cells (n=3 mice, 7 slices). **F** Control experiment for mouse *Ndnf in situ* with a negative probe (6 slices from 3 mice). **G to J** Due to the strong autofluorescence of human tissue, we performed chromogenic rather than fluorescent *in situ* hybridization. **G** Control experiment for human *in situ* shows little unspecific labeling (5 slices from 2 patients). **H** Slice of human temporal cortex showing chromogenic *in situ* hybridization for *NDNF*, and quantification of expression profile along the depth in cortex (same as **Figure 4**, displayed

here for comparison, 12 slices from 2 patients). **I** Expression of *VIP* is low in layer 1, and shows a peak in upper layer 2 (10 slices from 2 patients), similar to the expression profile in mouse neocortex (**Figure 2**). **J** Expression of *HTR3A* receptors resembles that of *VIP*, consistent with co-localization of these markers (same as **Figure 2**, displayed here for comparison 9 slices from 2 patients). Together, these data indicate that in both species *NDNF* is a selective marker for layer 1 interneurons, that *VIP* and *HTR3A* receptors are restricted to a small subset of L1-INs, and that they potentially co-localize as our recordings in the mouse suggest (**Figure 2**). Error bars indicate s.e.m. The images in panels **G** to **J** are a montage of images stitched using Pannoramic Scan software.

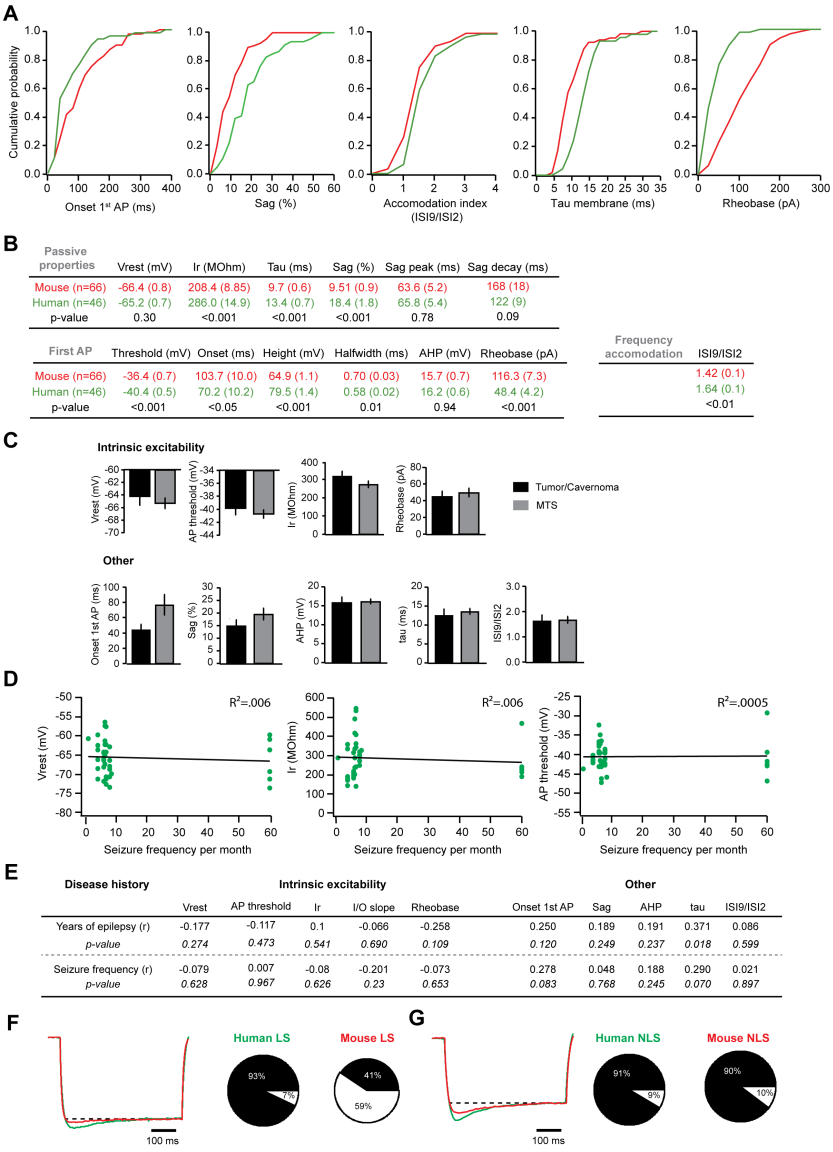

Figure S4: Cellular properties of human and mouse layer 1 interneurons, and further analyses of the impact of* disease type or disease history of the human patients. *Related to Figure 3.

Cumulative distributions (**A**) and table (**B**) summarizing the electrophysiological properties of human (n=46) and mouse (n=66) layer 1 interneurons (**B:** all values are presented as mean and s.e.m., p-values are the result of Kruskal-Wallis tests). We observed differences between human and mouse L1-INs in a number of parameters: Human L1-INs displayed higher input resistance, slower membrane time constant, larger voltage sag as determined by the percentage difference between the steady-state and peak voltage during a hyperpolarizing current step, more hyperpolarized action potential threshold, shorter onset of firing the first action potential at rheobase, greater action potential amplitude, faster action potential kinetics, lower rheobase and a higher level of accommodation during trains of action potentials (>20 Hz) as determined by dividing the 9th inter-spike interval by the second. **C** Data from patients with mesial temporal sclerosis (light grey, 36 neurons from 8 patients) and from patients which had epilepsy as a result of tissue malformation (tumor or cavernoma, dark grey, 10 neurons from 3 patients) were compared. No significant differences were found for the different parameters investigated between these groups (Vrest: -65.4±0.8 vs -64.1±1.6

mV, p=0.44; AP threshold: -40.6±0.6 vs -39.7±1.1 mV, p=0.39; input resistance: 277.2±16.7 vs 317.5±27.1 MΩ, p=0.14; rheobase: 49.3±5.1 vs 45±6.2 pA, p=0.99; onset latency 1st AP: 77.4±12.7 vs 44.5±6.8 ms, p=0.39; sag: 19.3±2.2 vs 15.0±2.4 %, p=0.5; AHP: 14.3±1.5 vs 15.8±1.5 mV, p=0.61; membrane time constant: 13.7±0.8 vs 12.5±1.6 ms; ISI9/ISI2: 1.64±0.13 vs 1.64±0.23, p=0.99). **D** We addressed the potential influence of disease severity on intrinsic excitability of layer 1 neurons. Correlations between seizure frequency per month and intrinsic excitability showed only very weak, non-significant correlations (resting membrane potential: R^2 =0.006, p=0.63, input resistance: R^2 =0.006, p=0.63, AP threshold: R^2 =0.0005, p=0.97). **E** Table summarizing correlations between neuronal parameters and disease state. With the exception of membrane time constant, we observe no correlation between disease history and intrinsic properties. This suggests that disease history is unlikely to have a major impact on the results. **F** A notable difference between human and mouse late-spiking cells is the larger voltage sag (p<0.001, Kruskal-Wallis test, human n=14, mouse n=37, 11.8±1.3 versus 6.1±0.9 %). Traces on the left are normalized to steady-state voltage to illustrate this. In addition, the proportion of late-spiking cells with a voltage sag >5% was also significantly greater in human L1-INs (black, p<0.01, Fisher's exact test). **G** While human non-late-spiking cells also showed larger voltage sag (left, p<0.01, Kruskal-Wallis test, human n=32, mouse n=29, 21.3±2.3 versus 13.8±1.3 %), the proportion of cells with a voltage sag >5% was similar for both species (black, p=0.99, Fisher's exact test). Error bars indicate s.e.m.

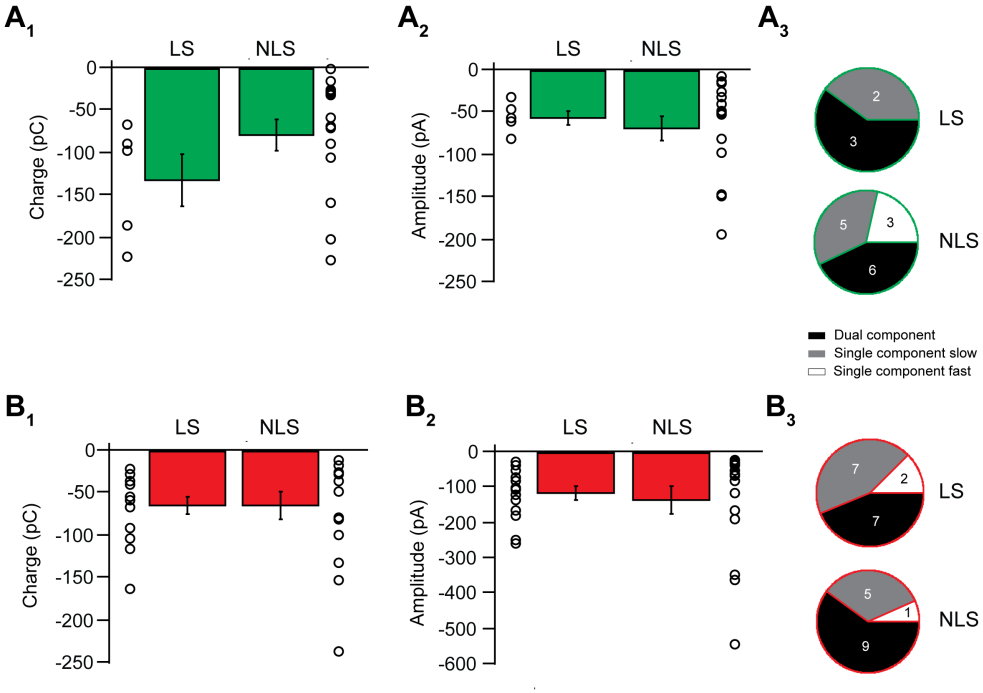

Figure S5: Nicotinic responses in non-late-spiking and late-spiking layer 1 interneurons. Related to Figure 3.

Nicotinic receptor responses were grouped for non-late-spiking (NLS) and late-spiking (LS) L1-INs (hierarchical clustering using Ward's method, **Figure 3**), and analyzed for charge, amplitude and receptor composition. **A_1, A_2** In the human, LS and NLS neurons showed similar response charge and amplitude (p=0.21, Kruskal-Wallis test, n=5 versus n=14, -133.0±29.9 pC versus -80.4±18.8 pC, and p=0.78, Kruskal-Wallis test, -56.4±8.2 versus -68.9±15.6 pA). **B_1, B_2** Similar analysis for mouse L1-INs. Comparable to the human, there was no detectable difference between LS and NLS cells (p=0.38, Kruskal-Wallis test, n=15 versus n=16, -65.0±10.9 versus -66.4±15.8 pC, and p=0.45, Kruskal-Wallis test, -117.6±18.0 versus -137.5±38.7 pA). **A_3, B_3:** Nicotinic response types found on late-spiking and non-late-spiking L1-INs. There was no detectable difference in the relative proportions of dual, single fast and single slow component responses in either species (human: p=0.58, mouse: p=0.72, Fisher exact test). Error bars indicate s.e.m.

Supplemental Experimental Procedures

Contact for reagent and resource sharing

Further information and requests for resources and reagents should be directed to and will be fulfilled by the lead contact, Johannes Letzkus (johannes.letzkus@brain.mpg.de).

Experimental model and subject details

Human brain tissue

Human brain tissue was obtained from 13 patients (10 male, 3 female, age range 19-52 years, age 36.6±2.9 years). Patients were either diagnosed with, and treated for, mesial temporal sclerosis (n=10), a brain tumor (n=2) or cavernoma (n=1). Healthy human brain tissue was obtained from anterior medial temporal cortex that had to be removed for surgical access to deeper brain structures (see below), with written informed consent of the patients before surgery.

Mouse brain tissue

Experimental mice (85±5 days, age range 40 to 162 days) of both sexes were either wildtype C57Bl6/J transgenes obtained from a cross of Vip-ires-cre (Taniguchi et al., 2011) with conditional tdTomato reporter animals (Ai9, Madisen et al., 2010) in C57Bl6/J background or NDNF-eGFP mice (Gong et al., 2003) in C57Bl6/J background. Mice were maintained in a 12 hour light/dark cycle, with access to food and water *ad libitum*.

Human slice preparation

All procedures on human tissue were performed with the approval of the Medical

Ethical Committee of the VU University Medical Centre, and in accordance with Dutch license procedures and the declaration of Helsinki. Human brain slices were cut from anterior medial temporal cortex tissue that had to be removed to provide surgical access to deeper brain structures, with written informed consent of the patients before surgery, as described previously (Testa-Silva et al., 2014). While precise information on the localization of the excised tissue was not available, the human anterior medial temporal cortex as a whole is an associative, multimodal area involved in associative learning. On this basis, as well as on the basis of homologous localization in as far as that is possible despite the expansion of temporal association areas during evolution (Squire et al., 2004), we performed comparison recordings from mouse temporal association cortex (TeA) and neighboring secondary auditory cortex (AuV, according to Paxinos and Franklin, 2008) as in previous work (Verhoog et al., 2013). We obtained tissue from 13 patients (10 male, 3 female, age 36.6±2.9 years). Patients were either diagnosed with, and treated for, mesial temporal sclerosis (n=10), a brain tumor (n=2) or cavernoma (n=1). In all patients, the resected neocortical tissue was located well outside the epileptic focus or tumor, and displayed no structural abnormalities in preoperative MRI investigations. Anesthesia was induced with fentanyl (1–3 µg/kg, i.v.) and a bolus dose of propofol (2–10 mg/kg), and was maintained with remyfentanyl (250 µg/kg/min) and propofol (4–12 mg/kg). After resection, the cortical tissue was placed within 30 s in ice-cold artificial CSF (aCSF) slicing solution, which contained the following (in mM): 110 choline chloride, 26 NaHCO3, 10 D-glucose, 11.6 sodium ascorbate, 7 MgCl2, 3.1 sodium pyruvate, 2.5 KCl, 1.25 NaH2PO4, and 0.5 CaCl2. The tissue was then transported to the neurophysiology laboratory, which is located within 200 m of the operating room. Transition time between resection of tissue and slice preparation was <10 min. Cortical slices (350 µm thick) were prepared in ice-cold slicing solution, and transferred to holding chambers in which they were stored for 30 min at 34°C and subsequently for at least 1 h at room temperature All aCSF solutions were

continuously bubbled with carbogen gas (95% O2, 5%CO2), and had an osmolality of 300 mOsm.

Mouse slice preparation

Experimental mice were either wildtype C57Bl6/J, or transgenes obtained from a cross of Vip-ires-cre (Taniguchi et al., 2011) and conditional tdTomato reporter animals (Ai9, Madisen et al., 2010) in C57Bl6/J background. Mice were maintained in a 12 hour light/dark cycle, with access to food and water *ad libitum*. All animal procedures were performed in accordance with institutional guidelines and were approved by the Regierungspräsidium Darmstadt. To ensure comparability to the human data, slices were obtained from temporal association cortex (TeA) and secondary auditory cortex (AuV, coordinates from bregma according to Paxinos and Franklin (2008): 2 to 3.2mm posterior, 4 to 4.5mm lateral, 2.5 to 3.6mm ventral) of adult male and female mice (85±5 days, age range 40 to 162 days). All recordings made to study nicotinic receptor currents used slicing solutions as reported above for human slice preparation. Slices in which serotonergic currents were studied were made using standard aCSF solution containing (in mM) 125 NaCl, 26 NaHCO3, 10 D-glucose, 7 MgCl2, 3 KCl, 1.25 NaH2PO4, and 0.5 CaCl2.

Patch-clamp recordings in human and mouse slices

Slices were transferred to the recording chamber and perfused with aCSF (2-3 mL/min). All experiments were performed at 31-34°C. Cells were visualized using differential interference contrast microscopy. Whole-cell voltage-clamp and current-clamp recordings were made using Multiclamp 700B amplifiers (Axon Instruments, CA), low-pass filtered at 5 to 20 kHz and digitized at 10 to 50 kHz (Digidata 1550, Molecular Devices) using pClamp software (Molecular Devices). Recordings were

rejected or terminated when the access resistance exceeded 20 MΩ. Patch pipettes (3-6 MΩ) were pulled from standard-wall borosilicate capillaries and were filled with intracellular solution (in mM): 140 K-gluconate, 1 KCl, 10 4-(2-hydroxyethyl)-1-piperazineethanesulfonic acid, 4 Na-phosphocreatine, 4 ATP-Mg, 0.4 GTP and biocytin (4 mg/mL). pH was adjusted to 7.3 with KOH, and osmolality was 290-300 mOsm. Layer 1 was identified by the lower cell density compared to layer 2/3. The L1/L2 border was defined by binning neuron density (bin size 10 µm), and identifying the last bin before the neuronal density exceeded 1 standard deviation above the average of the first 250 µm for 3 consecutive bins in human slices, and above the average of the first 80 µm for 2 consecutive bins for mouse tissue. To avoid recording neurons from a mixed L1-L2 population, cells were only recorded if they were located >20 µm from the L2 border, which was verified in a subset of the experiments by post hoc staining for NeuN and biocytin. TdTomato labeled Vip neurons were visualized under epifluorescence using an LED (565 nm, Cool LED) and a CCD camera (Infinity3, Lumenera). When the whole-cell configuration was established, hyperpolarizing and depolarizing current steps of 500 ms duration were injected, starting at -100 pA with a step increment of 25 pA. From this data passive and active properties of the neuron were determined offline. Series resistance was left uncompensated, and values were not corrected for the liquid junction potentials. Fast ionotropic receptor currents on interneurons were tested in voltage clamp mode (-70 mV holding potential) by local pressure ejection of agonists from a glass pipette with a tip diameter of approximately 1 µm using either a Picospritzer III (General valve corporation, Fairfield, NJ) or a PDES-02DE-LA-2 pressure ejection system (NPI, Germany). Nicotinic currents were evoked by a 100 ms puff of acetylcholine chloride (Ach, 1 mM) with a pressure of 10psi. Despite the fact that rodent L1-INs display gap junction coupling (Chu et al., 2003, Tasic et al., 2016), previous research indicates that electrical synapses contribute little to nicotinic currents in L1-INs (Bennett et al., 2012, Chu et al., 2003), suggesting that the observed responses are

mediated by nicotinic receptors in the recorded neuron. Htr3 currents were tested using mChlorophenylbiguanide hydrochloride (mCPBG, 100μM, in a subset of mouse experiments depicted in **Figure 2** the concentration of mCPBG was changed to 1μM (n=2) or 10μM (n=2)), and application lasted 100 ms in mouse and human experiments. In a subset of human recordings in **Figure 2**, mCPBG was applied for either 1 or 10 seconds. In the experiment where L1 Vip negative and Vip positive cells are compared for modulation by Htr3 receptors, mCPBG and serotonin hydrochloride (5HT) were applied for 1 second. 5HT (100μM) was applied to human cells for a duration of 10 s. In a subset of human cells that did not show a depolarizing current to mCPBG or 5HT, nicotinic responses were tested and found in all cases. For 100 ms application the puffer pipette was located approximately 20 μm from the soma, while for longer application times the distance was increased to approximately 30-50 μm. All experiments were performed in the presence of DNQX (10 μM) and bicuculline freebase (1 μM) to block glutamatergic and GABAergic synaptic transmission. We note that while bicuculline freebase at very high concentrations has been reported to block small-conductance calcium-activated potassium channels in addition to ionotropic GABA receptors (IC_{50} > 46μM) (Khawaled et al., 1999), our main aim here was a species comparison and given that bicuculline was present in all mouse and human recordings this does not have a major impact on the comparability of these data-sets. The presence of atropine (400 nM) prevented stimulation of muscarinic receptors during acetylcholine application. The pH of the extracellular recording solution was measured after addition of the different drugs we used, and found to be unchanged at 7.35.

Intrinsic property analysis

The membrane time constant was determined by fitting a single exponential from the start of the current injection to the maximum voltage deflection in a hyperpolarizing

step of -50 pA. The voltage sag was calculated as the percentage difference between the maximum and sustained membrane potential from the first sweep that hyperpolarized the cell to more then -80 mV. Time of voltage sag peak was calculated as the time from the onset of current injection to the maximum voltage deflection. Subsequently the decay time constant of the voltage sag was determined by a single exponential fit from the determined peak to the end of the hyperpolarizing current pulse. A cell was considered to have a voltage sag if the peak exceeded 5% of steady-state voltage. Input resistance was determined by a linear fit through the IV curve of all passive steps. Spike frequency adaptation was calculated from the first sweep where the cell fired >20 Hz on average, by dividing the ninth inter-spike interval (ISI) by the second inter-spike interval. AHP amplitude was determined as the difference between action potential threshold and the minimal potential reached in the repolarizing phase of the action potential (50 ms window). AP threshold was defined as 10 mV/ms in the first derivative of the membrane potential. Action potential height was measured from threshold to the maximal voltage reached. Halfwidth was determined as the full width at half maximal amplitude. Passive and active properties were analyzed using Matlab scripts (Mathworks) and Clampfit (Axon Instruments).

To determine whether the disease history of human patients had an impact on these results, we addressed whether intrinsic properties are affected by the severity of the disease in terms of number of seizures per month, by the time the patients suffered from epilepsy prior to surgery or by disease type (8 patients suffered from mesial temporal sclerosis, 2 from a brain tumor and 1 from cavernoma). With the exception of membrane time constant, we find no such correlations in our data-set, and no significant differences between disease types (**Figure 3D** and **S4**). Moreover, recordings from neurons directly in the epileptic focus, which would be expected to show more severe changes than the neurons in healthy neocortex recorded here,

have suggested no change in action potential threshold (Beck and Yaari, 2008), together indicating that disease history has no major impact on these results.

Unsupervised cluster analysis

To test whether sub-types of L1-INs can be identified, we asked whether electrophysiological parameters can be grouped into distinct clusters. We used Ward's method, because it has no a priori assumption on the number of clusters to be formed. For analysis we used a broad set of electrophysiological properties described in **Figure 3** and **S4**. (Dis)similarity between cells was calculated by determining the Euclidean distance, whereafter cells in close proximity are paired and subsequently grouped into a hierarchical cluster tree. To generate equal weight for the different electrophysiological properties in calculating Euclidean distances, all parameters were first normalized by ranking them between 0 and 1. Cluster analysis was performed in Matlab.

Voltage clamp drug application data analysis

The charge of nicotinic currents was determined by calculating the area under the curve from the start of the current until it decayed back to baseline. Fast and slow nicotinic receptor currents were separated by eye, and post hoc analysis revealed two completely non-overlapping rise slope distributions which differed more than an order of magnitude in size. Together with the results of the pharmacology experiments (Methyllycaconitine citrate, MLA, 10 nM, for antagonizing α7 nAChR and dihydro-β-erythroidine hydrobromide, 1μM, for blocking β2-containing nAChRs), this allowed a reliable classification of fast, slow and biphasic nicotinic receptor compositions. To determine the rise time of the first peak that is mediated by fast α7 receptors, pure α7 and combined biphasic α7/β2 currents were pooled for analysis.

The rise time of β2-mediated currents was quantified on slow monophasic currents, whereas for the decay time pure β2 and α7/β2 currents were combined. For comparability and to avoid influence of the fast component, all β2 decay times were determined starting 400 ms after onset of the current, a time when α7 receptors contribute little to the response (see **Figure S1**). The charge of Htr3 currents was calculated from a fixed 3s interval, to be able to compare it to Htr3 negative cells. Charge and amplitude were calculated using Clampfit (Axon instruments).

In situ hybridization for Htr3a receptors in mouse

Adult mice were anesthetized with 4% isoflurane followed by intraperitoneal administration of ketamine (300 mg/kg) and xylazine (20 mg/kg), and perfused with ice-cold, oxygenated aCSF (in mM): 125 NaCl, 3 KCl, 1.25 NaH2PO4, 3 MgSO4, CaCl2, 26 NaHCO3, and 10 glucose (300 mOsm) for 5 minutes. After removal from the skull, the brain was drop-fixed for 1.5 hours in PLP fixative (4% paraformaldehyde, 5.4% glucose (wt/vol), 0.01 M sodium metaperiodate in lysine-phosphate buffer), washed and stored in RNAse free PBS.

For detection of *Htr3a* mRNA, 30 µm slices were cut from the temporal lobe of the neocortex using a microtome (Leica VT1200 S), and incubated with custom-made hybridization probes (Affymetrix, *Htr3a* receptor, Accession number: NM:001099644; *Htr3a* receptor (negative control), Accession number: NM:013561-N; β-actin, Accession number: NM:007393) followed by amplification steps for detection of labeling. For this we followed the manufacturer's protocol QuantiGene ViewRNA ISH Cell Assay for Fluorescence RNA *in situ* Hybridization (RNA FISH) with a few modifications: Detergent solution was added for 15 min at room temperature and washing steps were increased to 3x10 min.

After probing for mRNA, slices were postfixed (10 min, PLP) and washed three times with 1x PBS. To determine layers and cell depth we stained the slices with mouse anti-NeuN (1:1000, Merck Millipore). Slices were submerged in blocking solution (4% goat serum in 1x PBS), for 1 hour at 21°C, followed by antibody incubation overnight at 4°C. After washing three times with 1x PBS, slices were incubated with secondary antibody (goat anti-mouse Alexa 488, 1:500, Thermo Fisher Scientific), washed again and mounted (Aqua-poly/Mount, Polysciences) on microscope slides.

In situ hybridization for detection of Ndnf in mouse

Adult mice were anesthetized with 4% isoflurane and decapitated. After removal of the skull the brain was placed in a mold, submerged in optimum cutting temperature formulation (Tissue-Tek) and stored at -80 degrees Celsius. Frozen brain sections of 10 µm thickness were made on a cryostat (Leica CM3050 S) and stored at -80 degrees Celsius. In preparation for staining, slices were fixed in PFA (4%), dehydrated, placed in a hydrophobic barrier and pretreated with protease according to the manufacturer's protocol. For detection of *Ndnf* mRNA, slices were incubated with custom-made hybridization probes (Advanced Cell Diagnostics, probe no. 447471-C2, *Ndnf*; 320881, negative control), followed by amplification steps for detection of labeling. For this we followed the manufacturer's protocol RNAscope fluorescent multiplex assay (Advanced Cell Diagnostics). To determine layers and cell depth we stained the slices with DAPI (1:1000, Thermo Fisher) after which they were mounted on microscope slides (EcoMount). We note that while *Ndnf* mRNA was also detected in cells lining blood vessels (c.f. Tasic et al., 2016), our analysis algorithm was designed to exclude these aberrant shapes on the basis of sphericity.

In situ hybridization for NDNF, VIP and HTR3A in human

Due to strong autofluorescence of human brain sections, we performed a chromogenic staining assay on human fresh frozen sections. Upon arrival of the fresh brain samples in the laboratory, they were prepared as described above for mice. In preparation for staining, slices were fixed in PFA (4%), dehydrated, placed in a hydrophobic barrier and pretreated with hydrogen peroxide and protease. For detection of *NDNF*, *VIP* and *HTR3A* mRNA, slices were incubated with custom-made hybridization probes (Advanced Cell Diagnostics, probe no. 495251, *NDNF*; 452751, *VIP*; 310681, *HTR3A*; 310043, negative control) followed by amplification steps for detection of labeling. For this we followed the manufacturer's protocol RNAscope 2.5 HD Detection Reagent - RED (Advanced Cell Diagnostics). To determine layers and cell depth we stained the slices with hematoxylin (50%, Sigma), after which they were mounted on microscope slides (EcoMount).

Imaging and analysis of in situ hybridization

Mouse sections

Imaging was performed using a Zeiss LSM 780/880 confocal laser scanning microscope using a 40x oil objective. Image analysis was done from confocal z-stacks (step size 1 µm). Labeled cells were detected using custom Matlab scripts. Due to the different staining patterns for the different labels (NeuN and *in situ*), two different algorithms were developed: NeuN immunocytochemistry: Due to the high cell density only a subset of the z-stack was used for cell-layer identification from the density of the NeuN staining (mean projection over three consecutive slices). This is the reason why not all *in situ* labeled cells appear in the NeuN-images (**Figure S3**). A band-pass filtered (Gaussian kernel, 1.5 – 10 pixel with 0.4 µm/pixel) version of the image was then thresholded and labeled for object identification. *In situ* hybridization

for *Htr3a* mRNA (see **Figure S3** for an example data set): A maximum projection of the image stack was calculated. A high-pass filter (50 pixels) was applied to compensate for intensity variations across the field of view (e.g. vignetting). In order to distinguish between unspecific background (isolated bright spots) and specific label (local accumulation of spots) and to detect nearby labels as one cell, a number of morphological operations were then applied (image closing (4 pixels), image opening (1 pixel), image closing (10 pixels)). The resulting image was thresholded, the same threshold was applied to samples labeled with anti-sense and sense probes. The resulting binary image was transformed into labeled objects. Object size (minimum number of pixels: 150) and additional object properties (circularity > 0.5, eccentricity < 0.9) were used to further refine the object selection. In order to calculate cell positions relative to the pia, a line was drawn manually along the pia (red line in **Figure S3**). To take the curvature of the pia into account, the depth of each object was calculated as the distance between its center (center of gravity of binary object mask) and the closest point on the “pia-line” (thin white lines in **Figure S3**).

Human sections

The complete mounted slices were scanned on a slide-scanner (PannoramicMIDI, 3DHistech) in transmission mode, and stitched during acquisition using Pannoramic Scan software. Data were exported as RGB tif-files. The locations of pia and of stained cells were marked manually in user-defined subregions. The distance of each cell to the pia was then calculated for each cell (see above, **Figure S3**), cell numbers were binned according to their depth and subsequently converted to cell densities (cells / mm^3) based on the size of the subregion and slice thickness.

Density of Vip *positive interneurons*

Vip-ires-cre mice were crossed with a tdTomato reporter line. From the resulting offspring 3 adult (>8 weeks of age) mice were anesthetized with 4% isoflurane followed by intraperitoneal administration of ketamine (300 mg/kg) and xylazine (20 mg/kg). Mice were perfused with 4% PFA in PBS solution and post-fixed in the same solution overnight at 4°C. Slices of 50 µm were cut on a vibratome, washed 4x in PBS and put in blocking solution (3% BSA, 0.2% Triton in PBS) for two hours. Slices were incubated in blocking solution containing mouse anti-NeuN (1:1000, Merck Millipore) overnight at 4°C. Hereafter, slices were washed 4x with PBS and incubated in blocking solution containing goat-anti-mouse-Alexa488 secondary antibody (Thermo Fisher Scientific) for two hours. After washing 3x in PBS, slices were mounted (HIGHDEF IHC Fluoromount, Enzo Lifesciences) on glass coverslips. For detection of Vip-tdTomato neurons and NeuN stained neurons we used the algorithm described in the *in situ* hybridization section.

Quantification and statistical analysis

Data-sets were first tested for the null hypothesis of normal distribution using the Kolmogorov-Smirnov test. Normally and non-normally distributed data were tested with parametric and non-parametric tests, respectively. Unpaired data sets were tested for significance using a two-sided Kruskal-Wallis test or a two-sided Student's t-test. Paired data-sets were assessed with a one-sided Wilcoxon signed-rank test. Differences in proportions were tested with the Fisher's exact test and the extended Fisher-Freeman-Halton test when evaluating proportions of the three types of nicotinic currents in **Figure 1**. A result was considered significant when the p-value was lower than 0.05. Since effect size was unknown, sample size could not be pre-specified. No randomization procedure or blinding of experimenter was used in the experimental design.

RESOURCE TABLE

REAGENT or RESOURCE	SOURCE	IDENTIFIER
Antibodies		
mouse anti-NeuN	Merck Millipore	MAB377
goat anti-mouse Alexa 488	Thermo Fisher Scientific	A-11001
Chemicals, Peptides, and Recombinant Proteins		
Antisense *Htr3a*	Affymetrix	NM:001099644
Sense *Htr3a*	Affymetrix	NM:013561-N
Antisense B-actin	Affymetrix	NM:007393
Antisense human *NDNF*	Advanced Cell Diagnostics	495251
Antisense human *VIP*	Advanced Cell Diagnostics	452751
Antisense human *HTR3A*	Advanced Cell Diagnostics	310681
Human negative control probe	Advanced Cell Diagnostics	310043
Antisense mouse *Ndnf*	Advanced Cell Diagnostics	447471-C2
Mouse negative control probe	Advanced Cell Diagnostics	320881
Experimental Models: Organisms/Strains		
C57Bl6/J	In house breeding	
Vip-ires-cre	In house breeding	IMSR_JAX:010908
Conditional tdTomato	In house breeding	IMSR_JAX:007909
NDNF-eGFP	In house breeding	MMRRC:030028-UCD
Software and Algorithms		
Matlab	Mathworks	www.mathworks.com
Other		

Supplemental References

Beck, H., Yaari, Y. (2008). Plasticity of intrinsic neuronal properties in CNS disorders. Nat. Rev. Neurosci. *9*, 357-69.

Bennett, C., Arroyo, S., Berns, D., Hestrin, S. (2012). Mechanisms generating dual-component nicotinic EPSCs in cortical interneurons. J. Neurosci. *32*, 17287-96.

Chu, Z., Galarreta, M., Hestrin, S. (2003). Synaptic interactions of late-spiking neocortical neurons in layer 1. J. Neurosci. *23*, 96-102.

Gong, S., Zheng, C., Doughty, M. L., Losos, K., Didkovsky, N., Schambra, U. B., Nowak, N. J., Joyner, A., Leblanc, G., Hatten, M. E., Heintz, N. (2003). A gene expression atlas of the central nervous system based on bacterial artificial chromosomes. Nature *425*, 917-25.

Khawaled, R., Bruening-Wright, A., Adelman, J. P., Maylie, J. (1999). Bicuculline block of small-conductance calcium-activated potassium channels. Pflugers Arch. *438*, 314-21.

Madisen, L., Zwingman, T. A., Sunkin, S. M., Oh, S. W., Zariwala, H. A., Gu, H., Ng, L. L., Palmiter, R. D., Hawrylycz, M. J., Jones, A. R., Lein, E. S., Zeng, H. (2010). A robust and high-throughput Cre reporting and characterization system for the whole mouse brain. Nat. Neurosci. *13*, 133-40.

Squire, L. R., Stark, C. E., Clark, R. E. (2004). The medial temporal lobe. Annu. Rev. Neurosci. *27*, 279-306.

Taniguchi, H., He, M., Wu, P., Kim, S., Paik, R., Sugino, K., Kvitsiani, D., Fu, Y., Lu, J., Lin, Y., Miyoshi, G., Shima, Y., Fishell, G., Nelson, S. B., Huang, Z. J. (2011). A resource of Cre driver lines for genetic targeting of GABAergic neurons in cerebral cortex. Neuron *71*, 995-1013.

Tasic, B., Menon, V., Nguyen, T. N., Kim, T. K., Jarsky, T., Yao, Z., Levi, B., Gray, L. T., Sorensen, S. A., Dolbeare, T., Bertagnolli, D., Goldy, J., Shapovalova, N., Parry, S., Lee, C., Smith, K., Bernard, A., Madisen, L., Sunkin, S. M., Hawrylycz, M., Koch, C., Zeng, H. (2016). Adult mouse cortical cell taxonomy revealed by single cell transcriptomics. Nat. Neurosci. *19*, 335-46.

Testa-Silva, G., Verhoog, M. B., Linaro, D., De Kock, C. P., Baayen, J. C., Meredith, R. M., De Zeeuw, C. I., Giugliano, M., Mansvelder, H. D. (2014). High bandwidth synaptic communication and frequency tracking in human neocortex. PLoS Biol. *12*, e1002007.

Verhoog, M. B., Goriounova, N. A., Obermayer, J., Stroeder, J., Hjorth, J. J., Testa-Silva, G., Baayen, J. C., De Kock, C. P., Meredith, R. M., Mansvelder, H. D. (2013). Mechanisms underlying the rules for associative plasticity at adult human neocortical synapses. J. Neurosci. *33*, 17197-208.